Check for updates

Advanced Materials

ADVANCED MATERIALS
www.advmat.de

RESEARCH ARTICLE

Tunable Hetero-Intercalated 2D Superlattice for Frustrated Kondo Triangles

Daiyue Li[1] | Xiangyu Hu[2] | Gang Wang[1] | Ruizi Zhang[3] | Xinxi Liu[2] | Kangdi Niu[1] | Zenglong Guo[1] | Xizhi Fu[4] | Jinbo Pan[3] | Shixuan Du[3] | Junwei Liu[4] | Yi Zheng[2] | Junhao Lin[1,5,6]

[1]State key Laboratory of Quantum Functional Materials, Department of Physics, and Guangdong Basic Research Center of Excellence for Quantum Science, Southern University of Science and Technology (SUSTech), Shenzhen, China | [2]School of Physics, and State Key Laboratory of Silicon and Advanced Semiconductor Materials, Zhejiang University, Hangzhou, China | [3]University of Chinese Academy of Sciences and Institute of Physics, Chinese Academy of Sciences, Beijing, China | [4]Department of Physics, Hong Kong University of Science and Technology, Clear Water Bay, Hong Kong, China | [5]Quantum Science Center of Guangdong-Hong Kong-Macao Greater Bay Area (Guangdong), Shenzhen, China | [6]Guangdong Provincial Key Laboratory of Advanced Thermoelectric Materials and Device Physics and Shenzhen Key Laboratory of Advanced Quantum Functional Materials and Devices, Southern University of Science and Technology (SUSTech), Shenzhen, China

Correspondence: Jinbo Pan (jbpan@iphy.ac.cn) | Yi Zheng (phyzhengyi@zju.edu.cn) | Junhao Lin (linjh@sustech.edu.cn)

Received: 21 October 2025 | **Revised:** 28 December 2025 | **Accepted:** 7 January 2026

Keywords: anomalous hall effect | CVD growth | kondo superlattice | non-magnetic Ta | tunable hetero-intercalated superlattice

ABSTRACT

With the successes of van der Waals heterostructures in unveiling exotic quantum states and enabling applications, direct fabrication of 2D superlattices beyond bulk limits is appealing. We realize an unprecedented 2D Kondo superlattice, Ta-NbS_2, consisting of two coupled metallic 1H-NbS_2 monolayers intercalated with growth-controlled periodic Ta sublattices. One-step CVD enables tunable periodicities, yielding three Ta-moment motifs: bulk-like simple triangular geometry of $\sqrt{3}a\times\sqrt{3}a$ (Type I), 2D spin-frustrated 4a×4a (Type II), and 2D saturated $3\sqrt{3}a\times3\sqrt{3}a$ (Type III). Beyond the logarithmic resistance upturn at Kondo temperature (T_K), we observe anomalous Hall effect evolution from single-impurity to coherent Kondo regimes, reflecting collective Ta-Kondo sublattice interactions. Carrier density modulation tunes the balance between Kondo screening and RKKY interactions, establishing 2D bilayer Ta-NbS_2 as an ultra-tunable 2D Kondo superlattice for correlated quantum phenomena, with potential applications in spintronics and quantum devices.

1 | Introduction

The remarkable variety and tunable nature of 2D materials have raised enormous research activities across interdisciplinary scientific domains [1–4]. Interest in the coherence effects of 2D superlattices is recently soaring, by engineering periodic modulations of diverse modifiable properties that superimpose upon the parent lattice [5]. Recent advancements unfold the structural construction and electronic property modulation of superlattices using methods such as moiré patterns [6, 7], twist stacking [8–10], and intercalation [11–14]. Highly tunable quantum states such as superconductivity and the anomalous quantum Hall effects, as observed in magic-angle graphene [1, 2, 4], exemplify the great potential of 2D superlattices. However, these bilayer moiré superlattices typically have rather weak van der Waals (vdW) interlayer interaction, while promoting direct charge exchange and orbital hybridization between heterogenous atomic layers are expected to transform the intrinsic structures and interlayer forces from weak vdW interactions to strong ionic or covalent bonds [15], and thus, create exotic quantum phases beyond the conventional

Daiyue Li, Xiangyu Hu, and Gang Wang contributed equally to this work.

© 2026 Wiley-VCH GmbH

superlattice paradigm. Intercalation stands out as a promising method for exploring unconventional strongly-coupled bilayer superlattices by introducing foreign atoms into the vdW gaps, providing unlimited possibilities to unlock previously unattainable properties in conductivity, optics, and magnetism by exploiting effects. Pioneering examples, such as heterodimensional VS_2-VS superlattice chains [12], Cr_xTe_y superlattices [16], monolayer phosphorene molecular superlattices [13], 2D self-intercalation TaS_2 [11], and cation-exchange magnetic intercalation superlattices [14], have emerged as unprecedented platforms for discovering quantum states in 2D superstructures.

By introducing intercalation foreign atoms, it may give rise to the Kondo effect—a complex quantum phenomenon that emerges due to many-body interactions between itinerant electrons and localized magnetic moments. Originally observed in diluted magnetic systems [17], the Kondo effect has recently regained intense research interests by introducing dimensionality control, which allows drastic modifications of the Kondo cloud's length and fine tuning of the intriguing interplay between the Kondo screening, the Ruderman–Kittel–Kasuya–Yosida (RKKY) interaction, and the inherent spin-orbit coupling parameters, etc [18]. In the context of 2D materials, it has primarily been associated with disorder-induced defects [19, 20] or interstitial magnetic atoms [21, 22]. Intriguingly, localized magnetic moments in a Kondo system can have indirect exchange coupling via conduction electrons by transferring spin polarization over long distances, a phenomenon known as the Ruderman–Kittel–Kasuya–Yosida interaction [23]. In Kondo systems, the RKKY interaction plays a significant role in shaping the electronic structures as well as the magnetic properties, as a result of the competition between the Kondo screening of localized magnetic moments and the long-range RKKY interaction. More importantly, many emergent quantum phenomena in strongly correlated electron physics, especially in heavy fermion metals, such as unconventional superconductivity or quantum critical behavior, are attributed to competing RKKY interactions and Kondo physics [24]. By further enforcing dimensionality control, quantum confinement is expecting to drastically change the interplay between the RKKY and Kondo screening mechanisms [18, 25], which in the 2D limit also becomes highly tunable by external forces. Although vdW superlattices have been extensively studied in recent years, 2D Kondo systems with fully controllable periodic superlattices of magnetically frustrated local moments are yet to be reported. Here, we will show a viable strategy of hetero-intercalated bilayer superlattices for studying the rich Kondo physics in the 2D limit.

2 | Results

2.1 | Hetero-Intercalated Bilayer Superlattices in Ta-NbS_2

In 1980, S. S. P. Parkin and R. H. Friend first discussed intercalation studies of bulk NbS_2 and TaS_2 by chemical vapor transport (CVT). They found that various 3*d* magnetic elements (V, Cr, Mn, Fe, Co, Ni) can be induced into these two parent compounds and produce new compounds with different magnetic behaviors and superlattice structures [26, 27]. To date, a variety of studies have reported the intercalation behavior of TaS_2 and NbS_2 [11, 21, 28–30]. However, the physical properties of 3*d*-intercalated NbS_2 and TaS_2 in the 2D limit, which are potentially novel 2D systems with strong interlayer coupling, has rarely been reported [31]. Equally important, the mutual integration or hybridization of these two inherently intercalating systems remains unexplored. This intriguing gap motivates us to investigate NbS_2–TaS_2 hybrid systems, aiming to construct novel vdw intercalated heterostructures with potentially emergent magnetic and electronic functionalities.

The Ta-NbS_2 superlattices were synthesized via a one-step molten salt-assisted chemical vapor deposition method using Ta_2O_5 and Nb_2O_5 as metal precursors (Figure S1). Optical microscopy reveals that the resulting domains predominantly exhibit triangular shapes, consistent with the intrinsic hexagonal symmetry of the parent materials (Figure 1a). Most remarkably, the as-synthesized Ta-NbS_2 superlattices through mixed precursor powders exhibit a pronounced thickness selectivity. Based on comprehensive thickness measurements and statistical analyses across different precursor ratios, our growth method shows a consistent preference for bilayer formation. In contrast, monolayer NbS_2 is obtained under identical growth conditions in the absence of Ta_2O_5 (Figure 1b). The preferential formation of a bilayer configuration is presumably due to the self-limiting growth [32], which also facilitates atomic structural interpretation. Based on our observations, the intercalation process likely occurs subsequent to the formation of the bottom NbS_2 monolayer, accompanying the deposition of the second NbS_2 layer (Figure S2). Notably, this intercalation is confined to bilayer samples; Raman mapping of thicker regions confirms the absence of Ta incorporation. (Figure S3). Our method is highly reproducible in synthesizing different types of Ta-NbS_2 superlattices, and the detailed growth parameters are summarized in Table S1. Large-area optical microscopy and atomic force microscopy (AFM) measurements are shown in Figures S4 and S5.

Due to Ta intercalation, the Raman spectra exhibit pronounced deviations from those of the parent NbS_2. A distinct peak at 172 cm^{-1} emerges at a Ta:Nb molar ratio of 1:4 (Figure 1c) that is absent in either pristine NbS_2 or TaS_2 (Figure S6), indicating the formation of new long-range ordering. As the Ta content increases, additional vibrational modes appear, reflecting the development of increasingly complex superlattice structures. At a ratio of 1:2.5, the 172 cm^{-1} mode broadens, and four new peaks emerge at 338, 376, 411, and 431 cm^{-1}. Further increasing the ratio to 1:2 yields additional weak modes in the 50–200 cm^{-1} range and a near-uniform intensity across the main peaks. Notably, the consistent formation of bilayer-thick superlattices across compositions, together with the well-defined Raman signatures, provides a robust platform for correlating structural modulation with device performance.

Figure 1d shows a scanning transmission electron microscopy (STEM) image acquired from the edge region of the bilayer sample, with the experimental details provided in Figure S7. The monolayer in Figure 1d corresponds to the 1H structure of NbS_2, while the bilayer region exhibits the AB' stacking configuration of Ta-NbS_2. The corresponding fast Fourier transform (FFT) image, shown in Figure 1e, clearly reveals the emergence of a new periodicity in bilayer Ta-NbS_2 distinct from the monolayer 1H-NbS_2, i.e., the occurrence of a superlattice. Figure 1f presents a magnified view of the monolayer, where Nb and S atoms

15214095, 2026, 12, Downloaded from https://advanced.onlinelibrary.wiley.com/doi/10.1002/adma.202520751 by jinbo pan - Institute Of Physics Chinese Academy Of Sciences , Wiley Online Library on [26/05/2026]. See the Terms and Conditions (https://onlinelibrary.wiley.com/terms-and-conditions) on Wiley Online Library for rules of use; OA articles are governed by the applicable Creative Commons License

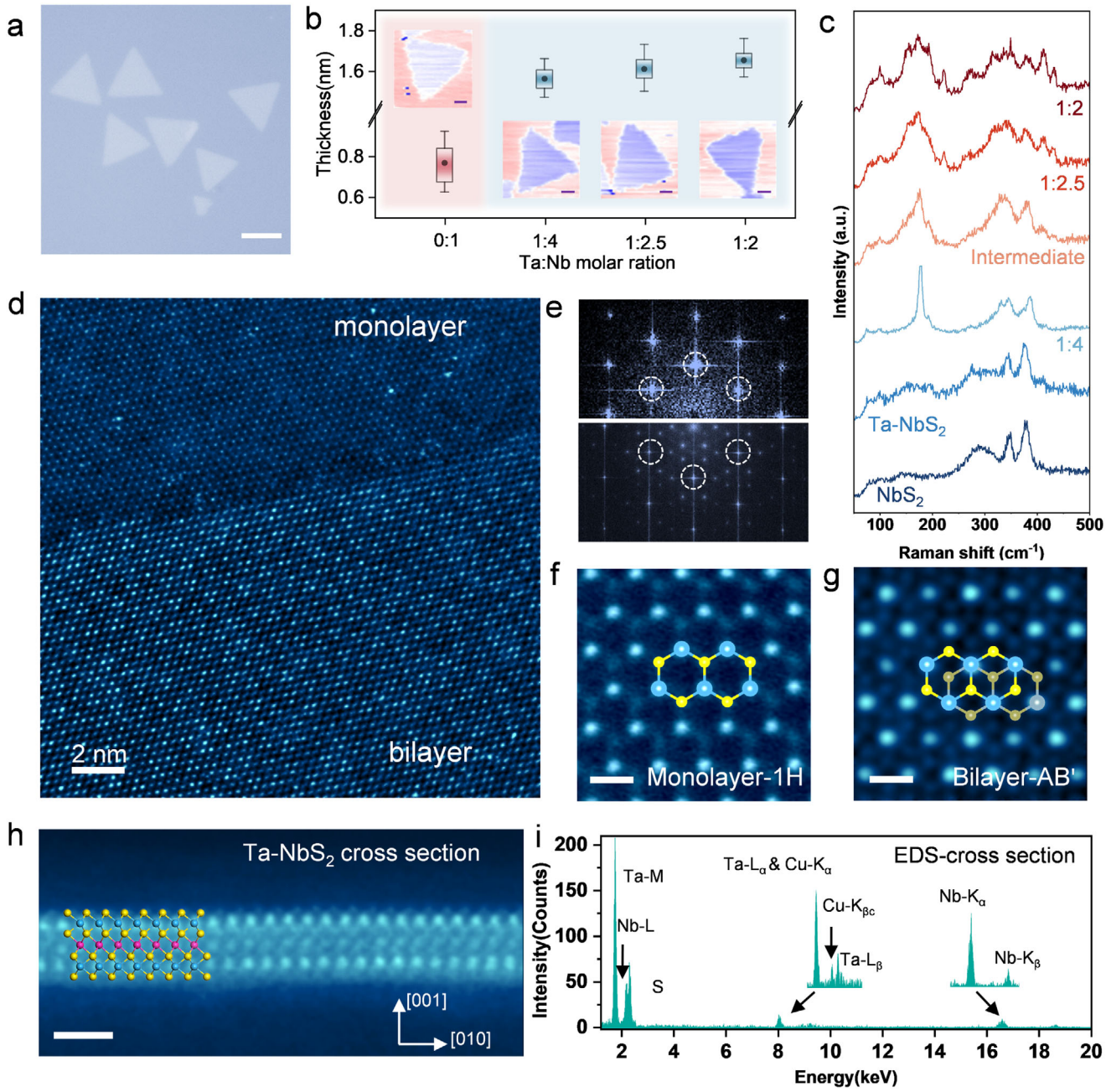

FIGURE 1 | Hetero-intercalation superlattices in Ta-NbS_2. (a) Optical image of Ta-NbS_2 superlattice flakes. (b) Thickness statistics of samples synthesized under different precursor ratios, showing a predominant bilayer configuration. (c) Raman spectrum of Ta-NbS_2 at different intercalation concentrations, exhibiting distinct Raman vibrational modes. (d–g) HAADF-STEM images of monolayer NbS_2 and bilayer Ta-NbS_2, showing a monolayer–bilayer contrast (d), the emergence of new periodicity in the FFT of the bilayer (e), the 1H structure of NbS_2 (f), and the AB' stacking of bilayer Ta-NbS_2 (g). (h) Cross- sectional STEM image of intercalation-grown 1L NbS_2/intercalated Ta /1L NbS_2, closely matching the overlaid atomic model. (i) Energy dispersion spectrum of Cross- sectional sample, including three kinds of elements: Ta, Nb, and S. Scale bars: (a) 10μm; (b) 1 μm; (d) 2nm; (f,g) 0.3nm; (h) 1nm.

form hexagonal rings with alternating contrast. In stark contrast, Figure 1g displays an enlarged view of the bilayer superlattice, where the brighter spots denote the AB' stacking Nb matrix, surrounded by dimmer spots of overlapping S columns, highly consistent with the contrast simulation (Figure S8).

To further substantiate the intercalated structure of Ta-NbS_2 bilayer superlattice, we utilized focused ion beam (FIB) to prepare cross-section samples (experimental details in Figure S9). In Figure 1h, a distinct intercalated atomic layer is clearly visible, with the up and down layers arranged in an anti-parallel manner, consistent with the structural characteristics of the AB' stacking configuration. Due to this unique stacking configuration, the inserted Ta atoms in the vdW gap form covalent bonds with six nearest neighboring sulfur atoms, producing an octahedral 1T-intercalation structure that is crucial for activating the Kondo physics. In the cross-sectional image, due to the higher abundance of niobium compared to the intercalated Ta, the contrast

15214095, 2026, 12, Downloaded from https://advanced.onlinelibrary.wiley.com/doi/10.1002/adma.202520751 by jinbo pan - Institute Of Physics Chinese Academy Of Sciences , Wiley Online Library on [26/05/2026]. See the Terms and Conditions (https://onlinelibrary.wiley.com/terms-and-conditions) on Wiley Online Library for rules of use; OA articles are governed by the applicable Creative Commons License

of Nb is noticeably stronger than that of Ta. Figure 1i represents the energy dispersive X-ray spectroscopy (EDS) spectrum of the cross-sectional STEM image. It is distinctive that only the Ta peak presents at the middle region, providing unambiguous evidence for the presence of uniform heterogeneous intercalation.

2.2 | Tunable Superlattice Structures Revealed by Atomic Characterization

The Ta intercalation ratio-dependent evolution in the Raman vibrational modes indicates that bilayer Ta-NbS_2 forms different superlattices with distinct Ta sublattice periodicities. Indeed, we have confirmed three types of bilayer superlattices associated with the aforementioned three characteristic Raman spectra. First, the Type I Ta-NbS_2 superlattice is characterized by the simple triangular intercalation bright spots observed in Figure 2a, with a stoichiometry of $Ta_1Nb_6S_{12}$. In this superlattice, Ta atoms occupy the corners of the supercell, forming a hexagonal supercell lattice of $\sqrt{3}a$, as illustrated in Figure 2d. By accommodating more interlayer Ta atoms, Type II superlattice emerges as shown in Figure 2b, where intercalated Ta atoms form a much-enlarged hexagonal supercell of $Ta_7Nb_{32}S_{64}$ (4a×4a), consisting of four single Ta vertices enclosing two mirror-symmetric trimeric Ta-clusters. As shown in Figure 2e,h, for the Type II supercell, the vertex Ta atoms retain the $\sqrt{3}a$ spacing from the nearest neighbouring Ta, while three Ta atoms within each trimer unit are close packed by sharing three pairs of 1T-TaS_6 octahedron edges. Such a unique vertex-trimer arrangement causes a four-fold expansion of the original NbS_2 lattice and produces the 4a×4a superlattice, in which the vertex "triangular" superlattice diffraction spots are clearly visible in the FFT analyses. Relevant atomic simulation images are provided in Figure S10, which show excellent consistence with the experimental data. The formation of the close-packing Ta trimers is also reflected in the Raman spectrum at Type II concentration (Figure 1c), which leads to an increased complexity of vibrational modes owing to the closer proximity and direct interactions among the Ta atoms. The emergence of distinctive trimeric intercalation units in Type II Ta-NbS_2 superlattice modifies the exchange interaction landscape.

Figure 2c represents the third superlattice structure with the highest Ta intercalation concentration, named the Type III Ta-NbS_2 superlattice. In this 2D saturation limit, all the intercalated Ta atoms form close-packed trimers, causing the supercell lattice to further expand to $3\sqrt{3}a \times 3\sqrt{3}a$ and a chemical stoichiometry of $Ta_{12}Nb_{54}S_{108}$. (Figure 2i) Interestingly, the minimum inter-trimer spacing also remains constant $\sqrt{3}a$, i.e. the nearest neighbouring non-close-packed Ta atoms are separated by two S columns. The complexity of this new periodicity is reflected in the corresponding FFT in Figure 2f, where additional superlattice diffraction spots show up. Due to the close packing trimer structure, the many-body interaction in Type III Ta-NbS_2 superlattice may become prevailed by the spin frustration effect of the Ta-trimers, a long-sought frustrated Kondo triangle system by various theoretical models [33–35]. The simulated diffraction patterns based on these superlattice models match well with the experiments (Figure S11). As shown in Figure S12, the atomic-scale lattice structures of the superlattices over a ~25 nm range demonstrate good translational symmetry. Raman mapping of the three superlattices further confirms uniformity on the micrometer scale (Figure S13). It is worth noting that the sparse trimers in the Type I lattice can be treated as dilute defect-like impurities, with negligible impact on the overall transport behavior. In addition, the intermediate state between Type I and Type II, which contains a higher density of trimers, exhibits distinct Raman features with a domain-like mixture of Type I and Type II superlattice, enabling clear identification (Figure S14). Note that both Type I and Type II exhibit C_6 symmetry, whereas Type III displays C_3 symmetry (Figure S15).

Although octahedral crystal field is allowed for three different bilayer stacking orders of AB', AB, and AA' [36], all three types of Ta-NbS_2 superlattices only exist in the AB' stacked bilayer structure of NbS_2, while no intercalation is observed in the AA' stacking (Figure S16) and only short-range $\sqrt{3}a$ periodicity of Ta intercalation can be found in the AB stacking regions (Figure S17). On the other hand, without well-defined octahedral crystal field sites, twisted NbS_2 bilayers also cannot accommodate Ta intercalation (Figure S18). Unlike AB and AA' bilayer, AB' stacking provides a highly symmetric coordination, wherein the Nb atoms of the top and bottom NbS_2 monolayers are positioned directly on each other. Such an energetically favorable environment promotes highly efficient intercalation and stabilizes the intercalated phase [29]. As an illuminating example, we show a Ta-NbS_2 bilayer with stacking order transitions from AB' to twisted structures (a stacking angle of 22°), separated by a transition zone of ~20 nm wide. Accordingly, changes in the stacking orders produce three distinctive Ta intercalation regimes from an ordered superlattice in the AB' regime, disordered intercalations in the transition zone, and no intercalations in the twisted regime, respectively (Figure S18). We thus infer that the balanced octahedron crystal field with minimal structural distortion of the AB'-NbS_2 bilayer phase is the key to realize the ordered intercalation superlattice. Equally important, unlike the conventional intercalation process, the superlattice formation with well-defined translational symmetry should be driven by thermodynamics, which occurs synchronously during the bilayer crystal growth.

Indeed, the experimentally observed Ta intercalation behavior in $Ta_xNb_yS_{2y}$ ($0 < x \leq 1/2y$) is further corroborated by density functional theory (DFT) calculations, by evaluating the formation enthalpies (ΔH) of various intercalated structures at representative compositions (Figure S19). The results are summarized in a ΔH vs Ta concentration ratio (defined by N_{Ta}:$N_{1/2Nb}$ = 2x/y) diagram (Figure 2j), referenced to decomposition into elemental Ta and pristine NbS_2 while the non-intercalated bilayer NbS_2 serves as the zero-energy baseline. For N_{Ta}:$N_{1/2Nb} \leq 0.33$, the intercalated Ta atoms favor singly dispersed configurations, without sharing 1T-TaS_6 octahedron edges. By further increasing the intercalation concentration, Ta atoms begin aggregating into close-packed trimeric units located at the energy minimums of the convex hull of the ΔH vs Ta concentration curve, including the experimentally observed Type II and Type III superlattices at N_{Ta}:$N_{1/2Nb}$ = 0.438 and 0.44, respectively. The thermodynamic stability of Ta trimers is attributed to enhanced in-plane orbital interactions and increased electronic delocalization, which concurrently stabilize the Ta—Ta bonding and reduce the density of

15214095, 2026, 12, Downloaded from https://advanced.onlinelibrary.wiley.com/doi/10.1002/adma.202520751 by jinbo pan - Institute Of Physics Chinese Academy Of Sciences , Wiley Online Library on [26/05/2026]. See the Terms and Conditions (https://onlinelibrary.wiley.com/terms-and-conditions) on Wiley Online Library for rules of use; OA articles are governed by the applicable Creative Commons License

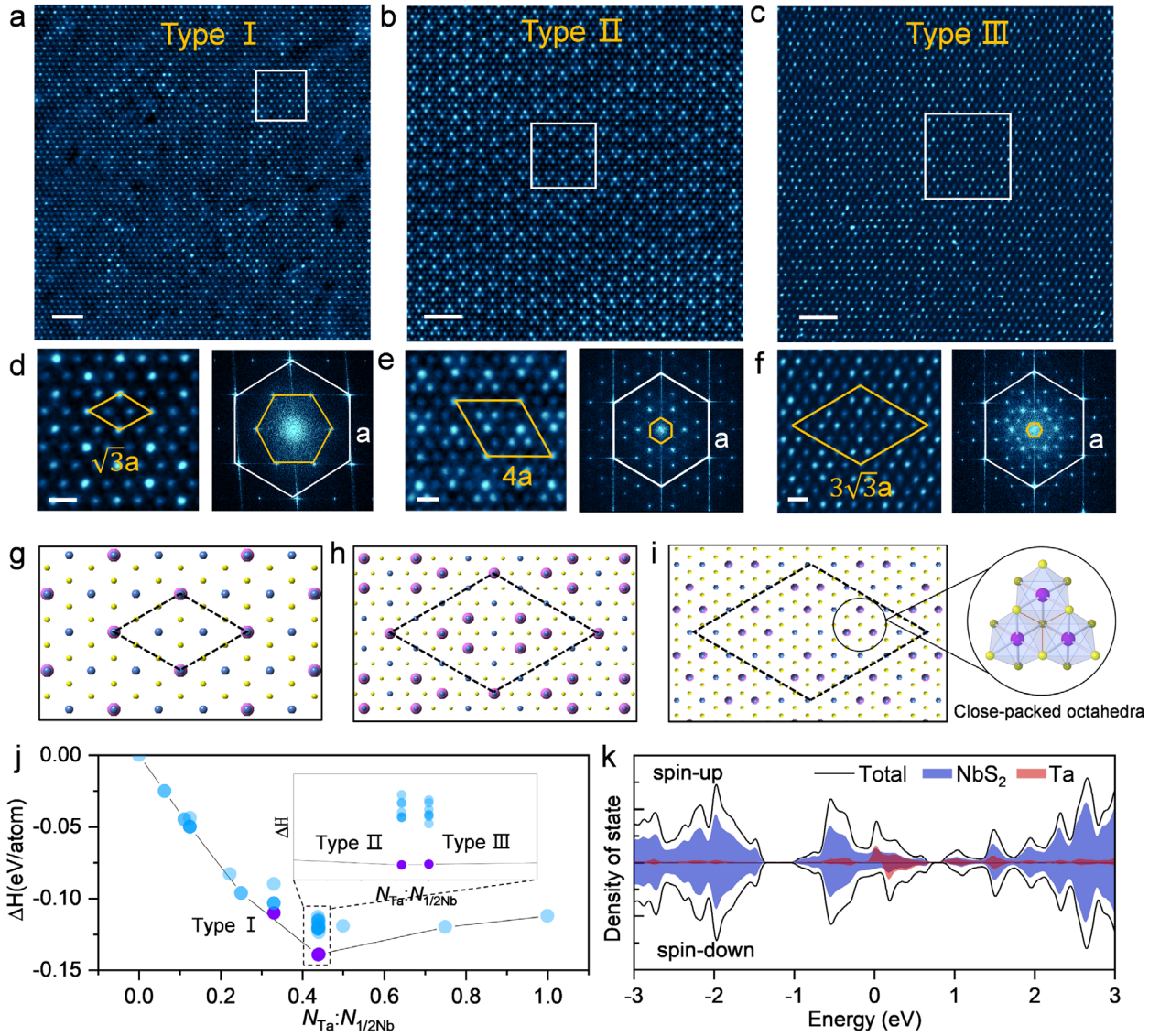

FIGURE 2 | Structure-associated superlattice formed by hetero-intercalated Ta atoms. (a–c) Atomic-resolution STEM-HAADF images of hetero-intercalated Ta-NbS_2, including concentrations of (a)Type I, (b) Type II, and (c) Type III Ta intercalated NbS_2. (d–f) Left, enlarged STEM images of the regions marked by white boxes in (a–c), along with the corresponding atomic structure models, which clearly exhibit the $\sqrt{3}a\times\sqrt{3}a$, $4a\times4a$, $3\sqrt{3}a\times3\sqrt{3}$ a superstructure, respectively. Right, the corresponding FFT patterns. (g–i) Atomic structure models of the three corresponding superlattices. The inset of (i) shows a close-packed arrangement of trimeric units with octahedral edge sharing. (j) The convex hull diagram of hetero-intercalated Ta-NbS_2, where purple spheres mark the formation energies of three superlattices. (k) Density of states of Ta-NbS_2, with the magnetic moment originating from the intercalated Ta atoms. Scale bars: (a–c) 2nm; (d–f) 0.5nm.

destabilizing states near the Fermi level compared to the singly dispersed configuration (Figure S20).

Theoretically, the direct consequence of the formation of 1T-TaS_6 octahedrons at the bilayer vdW gap is the emergence of localized Ta magnetic moments on the intercalation sites. These moments are predominantly associated with the Ta 5*d* orbitals, as revealed by the spin-resolved and orbital-projected band structures in Figure 2k and Figure S21. The local magnetic moments exhibit distinct magnetic configurations. In the Type I singly dispersed configuration, the intercalated Ta atoms exhibit long-range ferromagnetic ordering as controlled by the RKKY interaction, which is consistent with previous results [11]. For higher intercalation concentrations that are not feasible in the bulk limit, the trimer configuration favors short-range in-plane magnetic ordering as a result of prevailing superexchange interactions within individual trimers [37]. Interestingly, DFT deduces various in-plane magnetic configurations for the Type II and Type III superlattices, including representative clockwise rotation patterns and in-out alignment modes, which are schematically illustrated by arrows in Figures S22 and S23.

2.3 | Quantum Transport Characteristics of the Ta-NbS_2 Bilayer Superlattices

To evince the unconventional magnetic ordering of intercalated Ta atoms, we further explore the temperature (*T*)- and

15214095, 2026, 12, Downloaded from https://advanced.onlinelibrary.wiley.com/doi/10.1002/adma.202520751 by jinbo pan - Institute Of Physics Chinese Academy Of Sciences , Wiley Online Library on [26/05/2026]. See the Terms and Conditions (https://onlinelibrary.wiley.com/terms-and-conditions) on Wiley Online Library for rules of use; OA articles are governed by the applicable Creative Commons License

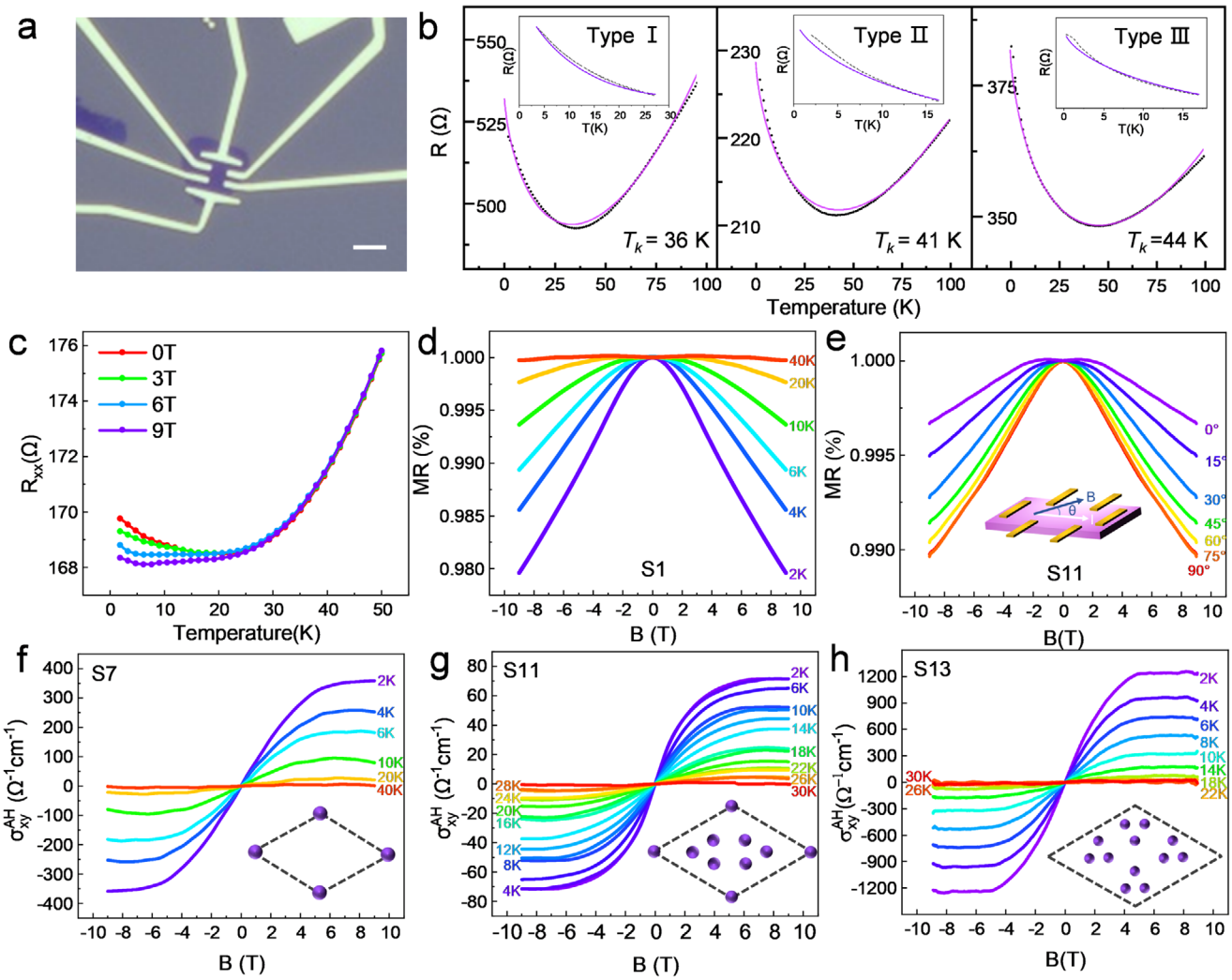

FIGURE 3 | Electrical Transport Characteristics of Ta intercalated NbS_2. (a) Optical microscopy image of a Ta-NbS_2 Hall bar device. Scale bar: 2μm. (b) Resistance as a function of temperature for three different Ta superlattice periodicities. The inset illustrates the clear deviation from the simple Kondo impurity model. (c) Logarithmic low-temperature-dependent resistance under different magnetic fields. (d) Out-of-plane magnetoresistance at different temperatures. (e) Magnetoresistance measured at different angles between the magnetic field and the sample plane (0° in-plane, 90° out-of-plane, as illustrated in the inset). Panels (c–e) show data from two distinct superlattice types: c from Type I and (d–e) from Type II. (f–h) Anomalous Hall effect signals for Type I (f), Type II (g), and Type III (h) Ta-NbS_2 superlattices, where the AHE is predominantly attributed to skew scattering.

angle-dependent magneto-transport properties of different types of Ta-NbS_2 bilayer superlattices. We measured the aforementioned superlattice samples utilizing the Hall-bar device geometry, as shown in Figure 3a, which are prepared by dry transferring followed by standard electron beam lithography (detailed damage-free transfer procedures from the growth mica substrate to the targeting silicon wafer can be found in the Methods section). Figure 3b compares the *T*-dependent longitudinal resistance (R_{xx}) of three types of Ta-NbS_2 bilayer superlattices. As illustrated in the insets, all three types of superlattice configurations exhibit pronounced logarithmic R_{xx} upturns below 60 K, hallmarking the onset of the Kondo effect [17]. As shown in Figure 3c, the resistivity upturn is suppressed by a strong magnetic field, suggesting two possible physical origins from the Kondo effect or weak localization. In contrast, electron–electron interaction–induced upturns are typically insensitive to magnetic fields. To exclude the weak localization contributions, we carried out magnetoresistance measurements with both in-plane ($B_{\parallel}$) and out-of-plane ($B_{\perp}$) magnetic field configurations. As summarized in Figure 3d,e, the results consistently exhibit negative magnetoresistance (NMR) behavior in the Ta-NbS_2 samples, providing decisive evidence on ruling out any potential correlation between the observed R_{xx} upturns and weak localization [38]. The quantum transport data are also consistent with the theoretical prediction that hetero-intercalated Ta introduces localized magnetic moments rooted in the 1T-TaS_6 octahedron crystal field (Figure 2k).

The prevalent Kondo effect in these Ta-NbS_2 bilayer superlattices can be consistently explained by the distinct prismatic and octahedron crystal field environments for Nb and Ta ions, respectively, when the highly symmetric AB' stacking configuration between two 1H-NbS_2 monolayers creates a unique 1T-type vdW cage for hetero-intercalating Ta atoms. The resulting crystal fields of TaS_6 octahedrons effectively isolate Ta ions from the metallic energy bands of 1H-NbS_2, creating localized Ta^{4+} mag-

15214095, 2026, 12, Downloaded from https://advanced.onlinelibrary.wiley.com/doi/10.1002/adma.202320751 by jinbo pan - Institute Of Physics Chinese Academy Of Sciences , Wiley Online Library on [26/05/2026]. See the Terms and Conditions (https://onlinelibrary.wiley.com/terms-and-conditions) on Wiley Online Library for rules of use; OA articles are governed by the applicable Creative Commons License

netic momentum of $S = 1/2$. For three different superlattices in Figure 3b, we readily fit the R_{xx}-T curves with the single-impurity Kondo model [39, 40]:

$$\rho(T) = \rho_0 + qT^2 + \rho_K \left\{ 1 - \ln\left(\frac{T}{T_K}\right) \left[ln^2\left(\frac{T}{T_K}\right) + S(S+1)\pi^2 \right]^{-\frac{1}{2}} \right\} \quad (1)$$

in which ρ_0 represents the residual resistivity, q accounts for the Fermi liquid contributions, T_K is the Kondo screening onset temperature, and S is the spin of the scattering magnetic momentum (see Methods for detailed fitting procedures). Agreeing with the DFT calculations, as illustrated in Figure S24, the best-fitting results for all three types of Ta-NbS_2 superlattices yield a spin state of $S = 1/2$, confirming the existence of local Ta^{4+}-magnetic moments associated with the TaS_6 octahedrons. The extracted $S = 1/2$ spin suggests the formation of Kondo magnetic impurities in all these Ta intercalated superlattices, which explains the underlying microscopic mechanism of the Kondo effect in Ta-NbS_2 bilayer superlattices (see Figure S25 for comparisons of the single-impurity Kondo model fitting with different values of S).

It is worth noting that the experimental data in Figure 3b exhibit discernible deviation from the single-impurity Kondo model at temperatures below 10 K, suggesting the emergence of non-negligible collective behavior of Kondo Ta^{4+} ions. Such a collective Kondo phenomenon can be mediated by the RKKY interaction of conduction electrons, i.e. coherent Kondo scattering [41], or more intriguingly, manifests the indirect exchange coupling between localized magnetic moments within the Kondo triangles [33–35]. We resort the anomalous Hall effect to probe the quantum signatures of the unconventional Kondo mechanism. As shown in Figure 3f–h and Figure S26 (in-plane B), for all three types of Ta-NbS_2 superlattices, the extracted AHE conductivity signals σ_{xy}^{AH} are robust below T_K and become saturated for high B setpoints (see Figure S27 for the extraction of AHE from the linear Hall backgrounds). The apparent T-dependence of σ_{xy}^{AH}, which vanishes when approaching T_K, correlates the AHE signals to the skew scattering mechanism. However, as shown in Figure 3g, a detailed analysis reveals that, below 10 K, the AHE conductivity of the Type II sample S11 does not exhibit a monotonic increase, which is typical for a dilute Kondo system with incoherent skew scattering. Conspicuously, the T-dependent AHE of S11 reaches a saturation value below 6 K, deviating from the paramagnetic Curie–Weiss limit (see Methods for fitting details). Considering the coexistence of singly dispersed and close-packed trimeric Ta in the Type II superlattice, such a notable deviation suggests the emergence of unconventional Kondo physics beyond the Kondo singlet limit [39, 40].

2.4 | Tunable AHE in Different Ta-NbS_2 Bilayer Kondo Superlattices

As illustrated in Figure 4a, in the single-impurity Kondo model, each local spin moment is individually screened by itinerant electrons to form Kondo singlets, which further form long-range indirect exchange coupling via the RKKY interactions. Utilizing T-dependent AHE, we get insights into the interplay between Kondo screening and the RKKY coupling, characterized by a pronounced transition from incoherent to coherent skew scattering that produces a σ_{xy}^{AH} maximum at a coherence temperature T_{coh} [41]. For a typical Kondo singlet system, T_{coh} is closely correlated to the carrier density, which regulates the Kondo screening for quenching the local magnetic moment fluctuations, and the RKKY coupling strength to mediate the Ta-sublattice band formation [42–44]. In Figure 4c, we compared two representative Type I samples with an order of magnitude difference in the hole concentrations, namely S7 (9.0×10^{13} cm^{-2}) and S12 (7.6×10^{14} cm^{-2}), respectively. With the same superlattice, the T-dependent evolution in σ_{xy}^{AH} of S7 follows the Curie-Weiss curve well, while S12 exhibits a distinctive incoherent-to-coherent transition at around 4 K.

By forming the close-packed Ta trimers, as schemed in Figure 4b, we introduce another tunable parameter of short-range antiferromagnetic coupling J_H between the close-packed TaS_6 octahedron trimers, realizing the long-sought Kondo triangle model with inherent spin frustration [33–35]. In Figure 4d, we show two representative Ta-NbS_2 bilayer samples for Type II (S11) and Type III (S13) superlattices, respectively. As evident by the robust σ_{xy}^{AH}, the close-packed Ta trimers are effectively screened by the 4d-conduction bands of the NbS_2 bilayer. Noticeably, the Type III superlattice (S13) follows the Curie-Weiss law very well, suggesting that Ta magnetic moments within different close-packed trimers are individually Kondo screened [39, 40], rather than prevailed by mutual entanglement to form a frustrated Kondo ground state [41]. Equally important, by increasing the Ta-intercalation density, we can see a clear trend of increasing T_K (Figures 3,b, and 4c), further confirming that the AHE measurements are in the Kondo singlet limit. To see the unconventional Kondo ground state, which requires $T_K/J_H \ll 1$, an efficient strategy is to reduce the conduction carrier density. Interestingly, with increased Ta intercalation, which are essentially electron donors to the hosting NbS_2 bilayer, the hole concentrations of Ta-NbS_2 superlattices show a systematic decrease (Table S2), providing a viable way for the further study of hetero-intercalated NbS_2 bilayer superlattices with well-controlled T_K /J_H ratios.

3 | Conclusion

In conclusion, we have experimentally demonstrated a viable hetero-intercalation strategy to directly synthesize 2D bilayer superlattices beyond the bulk thermodynamic limit, with long-range frustrated magnetic ordering as well as well-defined supercell parameters and symmetries. Utilizing DFT calculations and quantum transport measurements, we reveal that the two 2D Ta-NbS_2 bilayer superlattices with close-packed Ta trimers provide the material realization of frustrated Kondo triangles for exploring frustrated Kondo physics beyond the Landau Fermi liquid paradigm. Our findings unequivocally show the great promises of realizing unique 2D superlattices that is not feasible by the bulk growth and mechanical-exfoliation methods.

4 | Methods

4.1 | Growth by CVD Method

The synthesis was carried out in a two-zone horizontal tube furnace using a chemical vapor deposition (CVD) method. Sulfur

15214095, 2026, 12, Downloaded from https://advanced.onlinelibrary.wiley.com/doi/10.1002/adma.202520751 by jinbo pan - Institute Of Physics Chinese Academy Of Sciences , Wiley Online Library on [26/05/2026]. See the Terms and Conditions (https://onlinelibrary.wiley.com/terms-and-conditions) on Wiley Online Library for rules of use; OA articles are governed by the applicable Creative Commons License

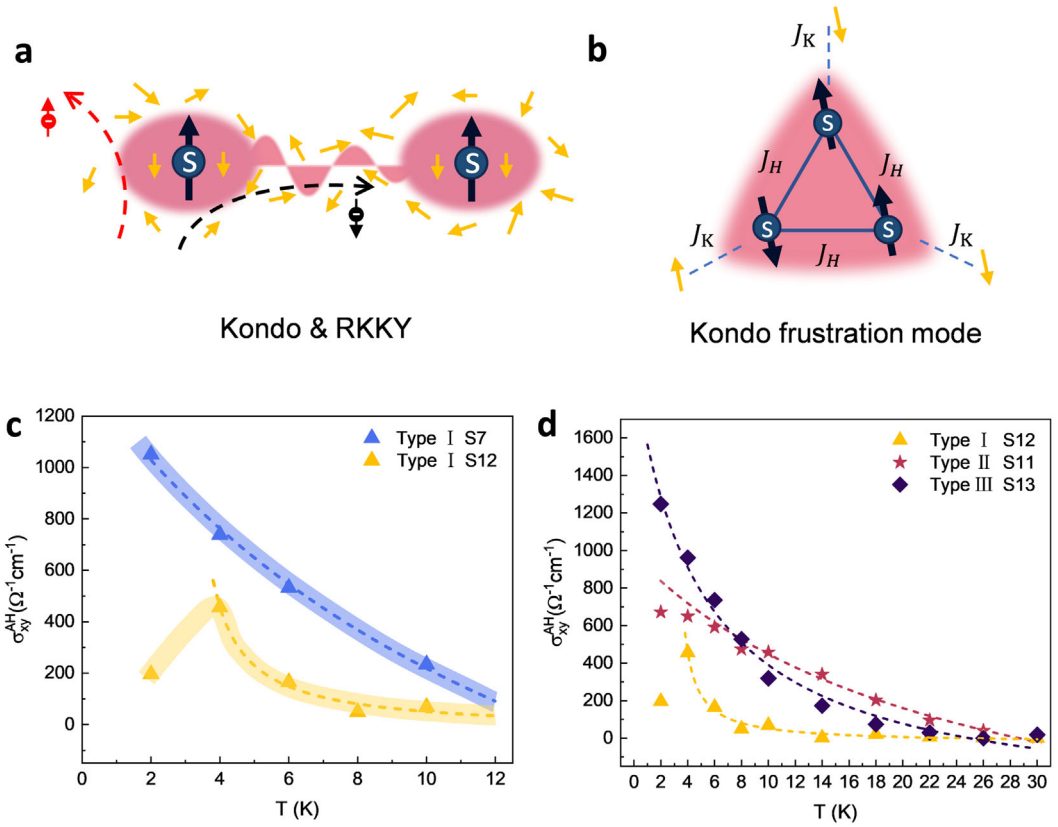

FIGURE 4 | Competition between the Kondo effect and RKKY physics in Ta-NbS_2. (a,b) Diagram of (a) RKKY interaction in the Kondo system and (b) the Kondo triangle model with inherent spin frustration. (c) Different saturated AHE behaviors observed in Type I Ta-NbS_2 due to the different conduction carrier density. (d) The saturated anomalous Hall signals at different temperatures, the dashed lines represent the fitting curves based on the Curie–Weiss law, while the experimental data are marked with different shaped points.

powder (100 mg) was loaded into an alumina boat and placed in the low-temperature zone of the furnace. Stoichiometric amounts of Ta_2O_5, Nb_2O_5, and NaCl powders were thoroughly ground and mixed, then transferred into a separate alumina boat positioned in the high-temperature zone. The furnace temperature was ramped at a rate of 40°C/min. When the high-temperature zone reached 400°C, the low-temperature zone was simultaneously heated to 180°C. The high-temperature zone was further heated to 700°C and held at that temperature for 10 min. During the entire process, a gas mixture of H_2 and Ar (30 sccm each) was continuously flowed through the system. Prior to the growth, the quartz tube was evacuated to a base pressure of 10^{-3} mbar and then refilled with high-purity Ar to ambient pressure. This purge-refill cycle was repeated twice to ensure a clean growth atmosphere. After the reaction, the furnace was opened, and the sample was rapidly cooled to room temperature using forced convection with a fan. The entire synthesis process of the superlattices was conducted within a glovebox-integrated system, ensuring that synthesis, characterization, and testing were all carried out under an inert atmosphere, thereby preserving the intrinsic lattice structure [45, 46].

4.2 | TEM Sample Preparation

The in-plane TEM specimen was prepared by a polymethyl methacrylate (PMMA)-assisted transfer method. A 3 μL droplet of PMMA solution was deposited onto the target area and baked at 80°C for 15 min to accelerate solidification. Subsequently, approximately 1 mL of deionized water was added around the edges of the PMMA film to initiate delamination from the mica substrate via surface tension. Additional water was supplied as needed to prevent evaporation and ensure continuous detachment. Once the PMMA film was fully separated, it was carefully lifted with tweezers and transferred onto a gold TEM grid with the carbon film facing upward. If alignment was suboptimal, a small amount of water was applied between the PMMA and the grid to assist with repositioning. Care was taken to keep the film flat to ensure uniform contact. After confirming proper adhesion, the sample was baked again at 80°C for 15 min to remove residual moisture. The grid was then immersed in acetone for 2 h to dissolve the PMMA, followed by rinsing in isopropanol (IPA) to reduce residual organic contaminants. Finally, the TEM grid was annealed in an ultra-high vacuum furnace at 320°C for 8 h to eliminate remaining organics and improve surface cleanliness for high-resolution TEM imaging. The transfer procedure onto a silicon substrate followed the same steps described above, except that the PMMA membrane was aligned and placed directly onto the target region of a clean SiO_2 wafer instead of a TEM grid. Both the 80 °C and 320°C heating steps used in the experiments do not damage the samples.

The cross-sectional TEM specimen was fabricated using a ThermoFisher Helios NanoLab 600i focused ion beam (FIB)

15214095, 2026, 12, Downloaded from https://advanced.onlinelibrary.wiley.com/doi/10.1002/adma.202520751 by jinbo pan - Institute Of Physics Chinese Academy Of Sciences , Wiley Online Library on [26/05/2026]. See the Terms and Conditions (https://onlinelibrary.wiley.com/terms-and-conditions) on Wiley Online Library for rules of use; OA articles are governed by the applicable Creative Commons License

system. Prior to FIB processing, a ∼100 nm graphite capping layer was transferred on the TaNbS flake within an N_2-filled glovebox to prevent environmental degradation and ion beam imaging damage. Subsequently, a 1–1.5 μm platinum-carbon (Pt-C) protective layer was deposited over the graphite layer to minimize ion beam-induced damage during milling. Cross-sectional lamellae with an approximate thickness of 50 nm were prepared along the direction perpendicular to the edge following standard lift-out protocols. Final thinning and surface damage removal were achieved through sequential Ga ion beam polishing at progressively reduced acceleration voltages of 5 and 2 kV.

4.3 | Scanning Transmission Electron Microscopy

Atomic structure characterization and elemental analysis were conducted using a FEI Titan Themis G2 double-aberration-corrected TEM equipped with a high-sensitivity super EDS detector. The accelerating voltage was set to 60 kV for in-plane flakes and 300 kV for cross-sectional specimens. HAADF imaging was performed with a collection angle ranging from 52 to 200 mrad, while the convergence semiangle was maintained at 30 mrad for both operating voltages. The beam current was optimized at approximately 30 pA for HAADF imaging and increased to 200 pA for EDS chemical mapping.

4.4 | Fabrication of Ta–NbS_2 Superlattice Devices

Ta-NbS_2 is subsequently transferred onto a Si/SiO_2 (295nm) substrate. Crystals with well-defined boundaries is chosen, and electron lithography, followed by thermal evaporation (3 nm Pd, 2nm Cr, and 35 nm Au), is employed to fabricate Hall bar-shaped contacts. The devices were then measured in a variable-temperature Cryogenic 9-T system using the standard four-probe technique with SR830 lock-in amplifiers. Experimentally, applying a gate voltage did not lead to a noticeable change in resistance, due to the relatively high carrier density of the metallic NbS_2 bilayer. The observed phenomenon is predominantly attributed to the skew scattering of conduction electrons by the localized Ta^{4+} ions. In these superlattices, the localized magnetic moments generated by the intercalated Ta ions create asymmetric scattering potentials, leading to preferential lateral deflection of conduction electrons and the emergence of a transverse Hall voltage.

4.5 | Single-Impurity Kondo Fitting of Ta-NbS_2

To avoid over-parameterization, ρ_0 is predetermined by extending the long-range linear portion in R-T curve to obtain the intercept, and S is fixed based on previously assumed hypotheses.

4.6 | DFT Calculations

Density functional theory (DFT) calculations in this study were performed using the Vienna Ab initio Simulation Package (VASP) [47]. The exchange–correlation interactions were treated within the generalized gradient approximation (GGA) using the Perdew–Burke–Ernzerhof (PBE) functional [48]. A plane-wave energy cutoff of 500 eV was employed, and the k-point sampling was chosen to ensure that the product of the lattice constant and k-point density in each reciprocal lattice direction exceeded 60 Å. Structural relaxations were carried out until the Hellmann–Feynman forces on each atom were less than 0.001 $eV \cdot Å^{-1}$, and the electronic self-consistency criterion was set to 10^{-6} eV.

For the construction of Ta-intercalated NbS_2 superlattices, Ta atoms were inserted between two layers of the H-phase NbS_2 monolayer. Various intercalation concentrations were simulated by using NbS_2 supercells of different sizes and varying the number of Ta atoms. A vacuum spacing of 20 Å was added along the out-of-plane direction to avoid spurious interactions between periodic images. For spin-polarized calculations, the initial magnetic configuration was set such that the intercalated Ta atoms were ferromagnetic, while the NbS_2 layers were initialized as non-magnetic.

Author Contributions

D.L. and J. Lin conceived the project idea. D.L. synthesized the superlattices, performed Raman spectroscopy and AFM characterizations, and conducted the analysis of STEM data. G.W. performed the STEM, EDX, and FIB measurements. K.N. contributed to part of the STEM data acquisition. Z.G. provided assistance and guidance on synthesis. Sample preparation and STEM characterization were supervised by J.L., X.H., and X.L. carried out device fabrication, measurement, and data analysis under the supervision of Y.Z. R.Z. performed the DFT calculations under the supervision of J.P. and S.D. X.F. provided a partial theoretical interpretation under the supervision of J. Liu. All authors contributed to the discussion of the results. Co-authors participated in writing the manuscript.

Acknowledgements

This work was supported by the National Key Basic Research and Development Program of China (Grant Nos. 2024YFA1409100, 2024YFA1408102 and 2023YFA1406302), Guangdong Major Project of Basic Research (2025B0303000004), the National Natural Science Foundation of China (Grant Nos. 52272146, 12374194, 52473302, 12404017, 12461160252, 12404018, U25A20386 and T2525009), Guangdong Basic Science Foundation (2023B1515120039), Guangdong Provincial Key Laboratory of Advanced Thermoelectric Materials and Device Physics (Grant No. 2024B1212010001), Natural Science Foundation of Guangdong Province, China (2025A1515011998), the Science, Technology and Innovation Commission of Shenzhen Municipality (No. ZDSYS20190902092905285), Shenzhen Natural Science Foundation (JCYJ20240813100412017) and Quantum Science Strategic Special Project (No. GDZX2301006), Shenzhen Municipal Funding Co-construction Program Project (No. SZZX2301004) from the Quantum Science Center of Guangdong-Hong Kong-Macao Greater Bay Area. STEM characterization was performed at the Pico Center from SUSTech Core Research Facilities that receives support from the Presidential Fund and Development and Reform Commission of Shenzhen Municipality.

Conflicts of Interest

The authors declare no conflicts of interest.

Data Availability Statement

The data that support the findings of this study are available from the corresponding author upon reasonable request.

15214095, 2026, 12, Downloaded from https://advanced.onlinelibrary.wiley.com/doi/10.1002/adma.202520751 by jinbo pan - Institute Of Physics Chinese Academy Of Sciences , Wiley Online Library on [26/05/2026]. See the Terms and Conditions (https://onlinelibrary.wiley.com/terms-and-conditions) on Wiley Online Library for rules of use; OA articles are governed by the applicable Creative Commons License

References

1. Y. Zhang, Y.-W. Tan, H. L. Stormer, and P. Kim, "Experimental Observation of the Quantum Hall Effect and Berry's Phase in Graphene," *Nature* 438 (2005): 201–204.

2. C. L. Kane and E. J. Mele, "Quantum Spin Hall Effect in Graphene," *Physical Review Letters* 95 (2005): 226801.

3. J. Fernández-Rossier and J. J. Palacios, "Magnetism in Graphene Nanoislands," *Physical Review Letters* 99 (2007): 177204.

4. Y. Cao, V. Fatemi, S. Fang, et al., "Unconventional Superconductivity in Magic-Angle Graphene Superlattices," *Nature* 556 (2018): 43–50.

5. Y. K. Ryu, R. Frisenda, and A. Castellanos-Gomez, "Superlattices Based on Van Der Waals 2D Materials," *Chemical Communications* 55 (2019): 11498–11510.

6. Y. Cao, V. Fatemi, A. Demir, et al., "Correlated Insulator Behavior at Half-Filling in Magic-Angle Graphene Superlattices," *Nature* 556 (2018): 80–84.

7. A. Jaoui, I. Das, G. Di Battista, et al., "Quantum Critical Behavior in Magic-Angle Twisted Bilayer Graphene," *Nature Physics* 18 (2022): 633–638.

8. Y. Li, F. Zhang, V.-A. Ha, and Y.-C. Lin, "Tuning Commensurability in Twisted Van Der Waals Bilayers," *Nature* 625 (2024): 494–499.

9. Z. Zhou, F. Hou, X. Huang, et al., "Stack Growth of Wafer-Scale Van Der Waals Superconductor Heterostructures," *Nature* 621 (2023): 499–505.

10. K. Zhang, Y. She, X. Cai, et al., "Epitaxial Substitution of Metal Iodides for Low-Temperature Growth of Two-Dimensional Metal Chalcogenides," *Nature Nanotechnology* 18 (2023): 448–455.

11. X. Zhao, P. Song, C. Wang, et al., "Engineering Covalently Bonded 2D Layered Materials by Self-Intercalation," *Nature* 581 (2020): 171–177.

12. J. Zhou, W. Zhang, Y.-C. Lin, et al., "Heterodimensional Superlattice With In-Plane Anomalous Hall Effect," *Nature* 609 (2022): 46–51.

13. C. Wang, Q. He, U. Halim, et al., "Monolayer Atomic Crystal Molecular Superlattices," *Nature* 555 (2018): 231–236.

14. J. Zhou, J. Zhou, Z. Wan, et al., "A Cation-Exchange Approach to Tunable Magnetic Intercalation Superlattices," *Nature* 643 (2025): 683–690.

15. Z. Wang, R. Li, C. Su, and K. P. Loh, "Intercalated Phases of Transition Metal Dichalcogenides," *SmartMat* 1 (2020): 1013.

16. B. Tang, X. Wang, M. Han, et al., "Phase Engineering of Cr_5Te_8 With Colossal Anomalous Hall effect," *Nature Electronics* 5 (2022): 224–232.

17. J. Kondo, "Resistance Minimum in Dilute Magnetic Alloys," *Progress of Theoretical Physics* 32 (1964): 37–49.

18. H. Prüser, et al., "Interplay Between the Kondo Effect and the Ruderman-Kittel-Kasuya-Yosida Interaction," *Nature Communications* 5 (2014): 5417.

19. J. H. Chen, L. Li, W. G. Cullen, E. D. Williams, and M. S. Fuhrer, "Tunable Kondo Effect in Graphene With Defects," *Nature Physics* 7 (2011): 535–538.

20. J. Ge, T. Luo, Z. Lin, et al., "Magnetic Moments Induced by Atomic Vacancies in Transition Metal Dichalcogenide Flakes," *Advanced Materials* 33 (2021): 2005465.

21. S. Shen, C. Wen, P. Kong, et al., "Inducing and Tuning Kondo Screening in a Narrow-Electronic-Band System," *Nature Communications* 13 (2022): 2156.

22. H. Liu, Y. Xue, J.-A. Shi, et al., "Observation of the Kondo Effect in Multilayer Single-Crystalline VTe_2 Nanoplates," *Nano Letters* 19 (2019): 8572–8580.

23. M. A. Ruderman and C. Kittel, "Indirect Exchange Coupling of Nuclear Magnetic Moments by Conduction Electrons," *Physical Review* 96 (1954): 99–102.

24. A. Schofieid, "Quantum Criticality in Metals," *Physics World* 16 (2003): 23–27.

25. A. Allerdt, A. E. Feiguin, and S. Das Sarma, "Competition Between Kondo Effect and RKKY Physics in Graphene Magnetism," *Physical Review B* 95 (2017): 104402.

26. S. S. Parkin and R. H. Friend, "3 d Transition-Metal Intercalates of the Niobium and Tantalum Dichalcogenides. I. Magnetic Properties," *Philosophical Magazine B* 41 (1980): 65–93.

27. S. S. Parkin and R. H. Friend, "3 d Transition-Metal Intercalates of the Niobium and Tantalum Dichalcogenides. II. Transport Properties," *Philosophical Magazine B* 41 (1980): 95–112.

28. Q. He, K. Si, Z. Xu, et al., "Direct Synthesis of Controllable Ultrathin Heteroatoms-Intercalated 2D Layered Materials," *Nature Communications* 15 (2024): 6320.

29. S. Wu, M. Dai, H. Li, et al., "Atomically Unraveling Highly Crystalline Self-Intercalated Tantalum Sulfide with Correlated Stacking Registry-Dependent Magnetism," *Nano Letters* 24 (2024): 378–385.

30. K.-T. Ko, K. Kim, S. B. Kim, et al., "RKKY Ferromagnetism With Ising-Like Spin States in Intercalated $Fe_{1/4}TaS_2$," *Physical Review Letters* 107 (2011): 247201.

31. Y.-L. Hong, Z. Liu, L. Wang, et al., "Chemical Vapor Deposition of Layered Two-Dimensional $MoSi_2N_4$ Materials," *Science* 369 (2020): 670–674.

32. Y. Su, E. Prestat, C. Hu, et al., "Self-Limiting Growth of Two-Dimensional Palladium between Graphene Oxide Layers," *Nano Letters* 19 (2019): 4678–4683.

33. K. Ingersent, A. W. W. Ludwig, and I. Affleck, "Kondo Screening in a Magnetically Frustrated Nanostructure: Exact Results on a Stable Non-Fermi-Liquid Phase," *Physical Review Letters* 95 (2005): 2–5.

34. B. Lazarovits, P. Simon, G. Zaránd, and L. Szunyogh, "Exotic Kondo Effect From Magnetic Trimers," *Physical Review Letters* 95 (2005): 1–4.

35. E. J. König, P. Coleman, and Y. Komijani, "Frustrated Kondo Impurity Triangle: A Simple Model of Deconfinement," *Physical Review B* 104 (2021): 115103.

36. H. J. Park, J. Cha, M. Choi, et al., "One-Dimensional Hexagonal Boron Nitride Conducting Channel," *Science Advances* 6 (2020): aay4958.

37. P. Zhang, M. Xue, C. Chen, W. Guo, and Z. Zhang, "Mechanism Regulating Self-Intercalation in Layered Materials," *Nano Letters* 23 (2023): 3623–3629.

38. B. L. Altshuler, D. Khmel'nitzkii, A. I. Larkin, and P. A. Lee, "Magnetoresistance and Hall Effect in a Disordered Two-Dimensional Electron Gas," *Physical Review B* 22 (1980): 5142–5153.

39. D. R. Hamann, "New Solution for Exchange Scattering in Dilute Alloys," *Physical Review* 158 (1967): 570–580.

40. T. Sekitani, M. Naito, and N. Miura, "Kondo Effect in Underdoped n-type Superconductors," *Physical Review B* 67 (2003): 174503.

41. N. Nagaosa, J. Sinova, S. Onoda, A. H. MacDonald, and N. P. Ong, "Anomalous Hall effect," *Reviews of Modern Physics* 82 (2010): 1539–1592.

42. J. Lu, A. H. C. Neto, and K. P. Loh, "Transforming Moiré Blisters Into Geometric Graphene Nano-Bubbles," *Nature Communications* 3 (2012): 823.

43. W. Zhao, B. Shen, Z. Tao, et al., "Gate-Tunable Heavy Fermions in a Moiré Kondo Lattice," *Nature* 616 (2023): 61–65.

44. J. Wu, Y. Liu, Y. Liu, et al., "Large Enhancement of Thermoelectric Performance in MoS_2/h-BN Heterostructure Due to Vacancy-Induced Band Hybridization," *Proceedings of the National Academy of Sciences* 117 (2020): 13929–13936.

45. Q. Yang, et al., "Unified Transmission Electron Microscopy With the Glovebox Integrated System for Investigating Air-Sensitive Two-Dimensional Quantum Materials," *Innovation* 6 (2025): 100751.

15214095, 2026, 12, Downloaded from https://advanced.onlinelibrary.wiley.com/doi/10.1002/adma.202520751 by jinbo pan - Institute Of Physics Chinese Academy Of Sciences , Wiley Online Library on [26/05/2026]. See the Terms and Conditions (https://onlinelibrary.wiley.com/terms-and-conditions) on Wiley Online Library for rules of use; OA articles are governed by the applicable Creative Commons License

46. Z. Guo, M. Han, S. Zeng, et al., "Intrinsic Grain Boundary Structure and Enhanced Defect States in Air-Sensitive Polycrystalline 1T″-WTe_2 Monolayer," *Advanced Materials* 36 (2024): 2402219.

47. G. Kresse and J. Furthmüller, "Efficient Iterative Schemes For Ab Initio Total-Energy Calculations Using a Plane-Wave Basis Set," *Physical Review B* 54 (1996): 11169.

48. J. P. Perdew, K. Burke, and M. Ernzerhof, "Generalized Gradient Approximation Made Simple," *Physical Review Letters* 77 (1996): 3865.

Supporting Information

Additional supporting information can be found online in the Supporting Information section.

Supporting File: adma72155-sup-0001-SuppMat.docx.

15214095, 2026, 12, Downloaded from https://advanced.onlinelibrary.wiley.com/doi/10.1002/adma.202520751 by jinbo pan - Institute Of Physics Chinese Academy Of Sciences , Wiley Online Library on [26/05/2026]. See the Terms and Conditions (https://onlinelibrary.wiley.com/terms-and-conditions) on Wiley Online Library for rules of use; OA articles are governed by the applicable Creative Commons License